CHINESE OPTICS LETTERS

Vol. 20, No. 8 | August 2022

# Zero field optically pumped magnetometer with independent dual-mode operation

Shaowen Zhang (张少文)[1,2,3], Jixi Lu (陆吉玺)[2,4*], Ying Zhou (周 莹)[2**], Fei Lu (逯 斐)[1], Kaifeng Yin (尹凯峰)[1], Di Zhan (詹 迪)[1], Yueyang Zhai (翟跃阳)[2,4], and Mao Ye (叶 茂)[2,4]

[1] School of Instrumentation and Optoelectronic Engineering, Beihang University, Beijing 100191, China

[2] Hangzhou Innovation Institute of Beihang University, Hangzhou 310051, China

[3] Beihang Hangzhou Innovation Institute Yuhang, Hangzhou 310023, China

[4] Research Institute for Frontier Science, Beihang University, Beijing 100191, China

*Corresponding author: lujixi@buaa.edu.cn

**Corresponding author: zhouyingphd@163.com

Received December 6, 2021 | Accepted May 7, 2022 | Posted Online May 26, 2022

We propose a dual-mode optically pumped magnetometer (OPM) that can flexibly switch between single-beam modulation mode and double-beam DC mode. Based on a 4 mm × 4 mm × 4 mm miniaturized vapor cell, the double-beam DC mode achieves a sensitivity of 7 fT/Hz$^{1/2}$ with probe noise below 4 fT/Hz$^{1/2}$ and working bandwidth over 65 Hz. This mode is designed to precisely measure the noise floor of a mu-metal magnetic shield. The single-beam modulation mode (sensitivity 20 fT/Hz$^{1/2}$) exhibits bandwidth characteristics suitable for biomagnetic measurements. Thus, our design is suitable for a miniaturized OPM with multiple functions, including magnetic-shield background noise measurement and medical imaging.

**Keywords:** optically pumped magnetometer; atomic optics; dual-mode magnetometer; magnetoencephalography; medical imaging.

**DOI:** 10.3788/COL202220.081202

## 1. Introduction

Optically pumped magnetometers (OPMs) operating in the spin-exchange relaxation-free (SERF) regime have been advanced significantly, owing to the demand for miniaturization, multichannel integration, low-cost manufacturing, and high sensitivity[1–4] of measurement tools for fundamental physics and biomagnetic detection[5–9]. Miniaturized SERF magnetometer arrays have been used in magnetocardiograms (MCGs) and magnetoencephalography (MEG) as an alternative for superconducting quantum interference devices[10,11].

SERF magnetometers have been investigated widely, which can be categorized into the double-beam mode (with pump and probe lights) and the single-beam mode (with only one pump light), based on the structure and detection principle used[12–14]. An ultra-high magnetic field sensitivity on the order of sub-femtotesla (fT) in a gradiometer arrangement with a spherical glass cell of 23 mm diameter using a double-beam mode SERF magnetometer has been reported by Dang *et al.*[15]. Colombo *et al.* developed a four-channel SERF magnetometer with a cross-sectional vapor cell area of 40 mm × 40 mm and reported gradiometric sensitivities of $< 5\,\mathrm{fT/Hz^{1/2}}$ at a bandwidth of approximately 90 Hz[16]. Wyllie *et al.* demonstrated that SERF magnetometers can be used for real-time fetal MCG detection with a single-channel sensitivity of approximately 5 fT/Hz$^{1/2}$ and a 1 cm$^2$ vapor cell[17]. We have previously demonstrated a single-channel sensitivity of 1 fT/Hz$^{1/2}$ with a 2.5 cm$^2$ vapor cell in the double-beam mode[18]. Therefore, the high sensitivity of the double-beam mode can be attributed mainly to larger vapor cells and gradient measurements. However, for miniature magnetometers with small vapor cells, obtaining a high sensitivity is still challenging.

Recently, single-beam mode SERF magnetometers have been applied widely in the field of biomagnetic measurement, owing to their suitable characteristics for miniaturization, array integration, and cost effectiveness. Osborne *et al.* have reported a zero field OPM for biomedical applications[19]. Vladislav *et al.* developed a multichannel system based on a SERF magnetometer with a microfabricated vapor cell and reported a noise floor below 20 fT/Hz$^{1/2}$[20]. In addition, a multichannel imaging system comprising 25 microfabricated OPMs with an average magnetic sensitivity of 24 fT/Hz$^{1/2}$ has been proposed previously, with a footprint of less than 1 cm$^2$[21,22]. Although the single-beam mode requires fewer optical components favorable for integration, it is difficult to achieve a noise floor lower than

$10\,\mathrm{fT/Hz^{1/2}}$ with millimeter (mm)-level vapor cells using the absorption detection method owing to laser noise.

In this study, we propose a dual-mode SERF magnetometer based on a $4\,\mathrm{mm}\times 4\,\mathrm{mm}\times 4\,\mathrm{mm}$ miniaturized vapor cell that can flexibly switch between the single-beam modulation mode and the double-beam DC mode. The double-beam DC mode is designed with suitable sensitivity to precisely measure the noise floor of a mu-metal magnetic shield, and the single-beam modulation mode exhibits bandwidth characteristics suitable for biomagnetic measurements. Our design is suitable for miniaturized OPMs with multiple functions, including magnetic-shield background noise measurement and medical imaging, which will aid in realizing portable magnetic sensing devices.

## 2. Principle of SERF Magnetometer

To calculate the spin polarization of alkali metal atoms, the Bloch equation is applied in the SERF regime[23]:

$$\frac{\partial P}{\partial t}=\frac{1}{q}[\gamma^e \boldsymbol{B}\times\boldsymbol{P}+R_{\mathrm{OP}}(s\hat{z}-\boldsymbol{P})-R_{\mathrm{rel}}\boldsymbol{P}], \tag{1}$$

where $\boldsymbol{P}=(P_x,P_y,P_z)$ is the electron polarization, $q$ is the slowing-down factor, $\gamma^e=2\pi g_s\mu_B/h=2\pi\times 28\,\mathrm{Hz/nT}$ is the electron gyromagnetic ratio, $\boldsymbol{B}$ is the magnetic field vector, $R_{\mathrm{OP}}$ is the pumping rate, and $s$ is the photon polarization of the pump light. $R_{\mathrm{rel}}$ is the transverse spin relaxation rate in the absence of light, dominated by spin destruction and wall collisions, which is given by[24]

$$R_{\mathrm{rel}}=R_{\mathrm{SD}}+\frac{1}{T_D}+\frac{1}{T_2^{\mathrm{SE}}}, \tag{2}$$

where $R_{\mathrm{SD}}$ is the spin-destruction relaxation rate, $1/T_D$ is the relaxation rate due to diffusion, and $1/T_2^{\mathrm{SE}}$ is the spin-exchange relaxation rate.

Assuming that the direction of the pump light is along the $z$ axis, the direction of the magnetic field to be measured is along the $x$ axis. When $B_y$ and $B_z$ are equal to zero, the steady-state components in Eq. (1) are given by[25]

$$P_x=0, \tag{3}$$

$$P_y=\frac{\gamma^e R_{\mathrm{OP}}}{(\gamma^e B_x)^2+(R_{\mathrm{OP}}+R_{\mathrm{rel}})^2}B_x, \tag{4}$$

$$P_z=\frac{R_{\mathrm{OP}}(R_{\mathrm{OP}}+R_{\mathrm{rel}})}{(\gamma^e B_x)^2+(R_{\mathrm{OP}}+R_{\mathrm{rel}})^2}. \tag{5}$$

Equations (4) and (5) describe the combined effects of the optical pumping and magnetic field on the polarization, represented by the spectrometric absorption ($P_y$) and dispersion ($P_z$) curves[26]. The magnetic field along the $x$ axis ($B_x$) can be detected using $P_y$ and $P_z$.

For the single-beam mode, the circularly polarized pump light along the $z$ axis is the only beam. When $B_x$ varies, the absorption exhibits a zero field Lorentz resonance, the half-width at half-maximum is $\Delta B_x=1/\gamma^e(R_{\mathrm{OP}}+R_{\mathrm{rel}})$, and the maximum value is proportional to $R_{\mathrm{OP}}/(R_{\mathrm{OP}}+R_{\mathrm{rel}})$. Then, a modulating magnetic field of amplitude $B_1$ and angular frequency $\omega$ is applied along the $x$ axis, $B_x+B_1\cos(\omega t)$. The response of $B_x$ in the zero field modulation mode can be described as a Fourier series. The dominant term in the solution is the first harmonic, as given by[26–28]

$$P_z(t)=k'\frac{R_{\mathrm{OP}}J_0\left(\frac{\gamma^e B_1}{\omega}\right)J_1\left(\frac{\gamma^e B_1}{\omega}\right)}{(\gamma^e B_x)^2+(R_{\mathrm{OP}}+R_{\mathrm{rel}})^2}\sin(\omega t)\gamma^e B_x. \tag{6}$$

Here, $J_n$ is the Bessel function of the first kind, and $k'$ is the constant of proportionality.

For the double-beam mode, a beam of linearly polarized probe light is added along the $y$ axis on the foundation of the single-beam mode. The rotation angle $\theta$ of the probe light is proportional to $P_y$. Equation (4) is approximately linear along the $x$ axis near $B_x=0$, and this component of the magnetic field may be extracted directly from the dispersive lineshape. The response of $P_y$ to the DC mode is given by Eq. (4).

During the operation of the dual-mode SERF magnetometer in the linear region, the term $(\gamma^e B_x)^2$ can be ignored when $R_{\mathrm{OP}}+R_{\mathrm{rel}}\gg\gamma^e B_x$. The polarizability of the $y$ axis and $z$ axis can be uniformly described by

$$P_{\text{single or double}}\approx\frac{R_{\mathrm{OP}}}{(R_{\mathrm{OP}}+R_{\mathrm{rel}})^2}\gamma^e B_x. \tag{7}$$

The polarizability ($P$) cannot be obtained directly, but instead the intensity of the laser is measured by photodiodes (PDs) as the response ($V$) of the magnetometer. From Eq. (7), we can further simplify the response as $V=k_{\text{double or single}}B_x$. Although the response has a similar form, the corresponding method of operation and scale factor $k$ are significantly different. In the balanced polarimetry technique, measuring the optical rotation angle can aid in achieving a higher magnetic field sensitivity, and, for lock-in amplifier demodulation polarization, it can effectively suppress low-frequency $1/f$ noise.

## 3. Experimental Setup

The experimental setup of the SERF magnetometer is illustrated in Fig. 1. The central part is a small-size alkali-metal vapor cell with external dimensions of $4\,\mathrm{mm}\times 4\,\mathrm{mm}\times 4\,\mathrm{mm}$ and interior dimensions $3\,\mathrm{mm}\times 3\,\mathrm{mm}\times 3\,\mathrm{mm}$, filled with a droplet of $^{87}$Rb and approximately 650 torr of $N_2$ as the buffer and quenching gas. The vapor cell was heated to approximately 150°C using a 200 kHz AC electronic current. The temperature was monitored and stabilized using a non-magnetic Pt1000 for real-time closed-loop control.

As shown in Fig. 1, when the SERF magnetometer operates in the single-beam mode, the pump light tuned to the Rb D1 resonance line is generated by a distributed feedback (DFB) laser.

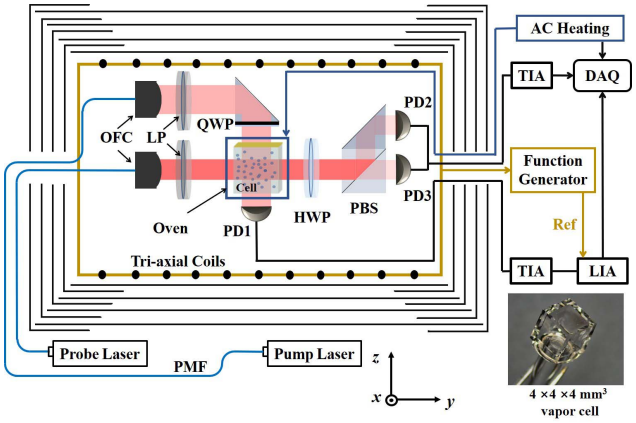


**Fig. 1.** Experimental setup of the SERF magnetometer for independent single-beam mode and double-beam mode operation. PMF, polarization maintaining fiber; OFC, optical fiber collimator; LP, linear polarizer; QWP, quarter-wave plate; PD, photodiode; HWP, half-wave plate; PBS, polarizing-beam splitter; TIA, transimpedance amplifier; LIA, lock-in amplifier; Ref, reference signal; DAQ, data acquisition.

The pump beam is delivered from the fiber collimator and circularly polarized by a set of linear polarizers and quarter-wave plates. After it is transmitted to the vapor cell, the pump light is detected by PD1 and converted into a voltage signal by an ultra-low-noise PD amplifier (Thorlabs, PDA200C). The lock-in amplifier (Zurich Instruments, MFLI) generates a modulated magnetic field with a frequency of $\omega = 1$ kHz along the sensitive $x$ axis and synchronously demodulates the magnetic field information detected by the PD.

When the SERF magnetometer operates in the double-beam mode, the pump light maintains the configuration in the single-beam mode. An additional probe beam is detuned to roughly 100 GHz from the Rb D1 resonance line. The probe beam passes through a fiber collimator and linear polarizer, yielding a linearly polarized beam. After passing through the vapor cell along the $y$ axis, the probe beam is geometrically split by a half-wave plate and a polarization beam splitter cube and detected using two PDs (PD2 and PD3). Through the balanced polarimetry technique, the difference between PD2 and PD3 outputs can be used as the response signal of the double-beam mode.

The modulation magnetic field (single-beam mode) and calibration magnetic field were added to the tri-axial coil through a summing amplifier. The output response signal was recorded using a data acquisition system (National Instruments, PXIe-4499). A four-layer cylindrical mu-metal magnetic shield was used to counteract the ambient magnetic field.

## 4. Results and Discussion

In this section, the SERF magnetometer performance in both modes was optimized separately. The laser frequency detuning and light intensity of the pump and probe lights were optimized first. Under the optimal light parameters, we discuss the optimal operating temperature to identify the optimal sensitivity and bandwidth.

### 4.1. Performance optimization

In the double-beam mode, the vapor cell is heated to 150°C, and the background magnetic field is compensated to zero by the tri-axial coil. The actual response signal ($V = k_{\text{double}} B_x$) is determined by the scale factor $k_{\text{double}} \approx k_1 k_2 k_3$, which is given by

$$k_1 = \eta_1 I_{\text{probe}}\, ln\, r_e c f_{D1} \gamma^e, \tag{8}$$

$$k_2 = \frac{\nu_{\text{probe}} - \nu_{D1}}{(\nu_{\text{probe}} - \nu_{D1})^2 + (\Gamma_{D1}/2)^2} e^{-\text{OD}(\nu_{\text{probe}})}, \tag{9}$$

$$k_3 = \frac{R_{\text{OP}}}{(R_{\text{OP}} + R_{\text{rel}})^2}, \tag{10}$$

where $\eta_1$ is the conversion factor of the balanced polarimetry detector, $I_{\text{probe}}$ is the probe light intensity, $l$ is the length of the vapor cell, $n$ is the atomic number density, $c$ is the speed of light, $f_{D1}$ is the oscillator strength, $\nu_{\text{probe}}$ is the frequency of the probe light, $\nu_{D1}$ is the resonant frequency of the Rb D1 line, $\Gamma_{D1}$ is the pressure-broadened absorption linewidth, and OD ($\nu_{\text{probe}}$) is the optical depth.

We first optimized the laser parameters of the probe light. The pump light frequency was maintained at the resonance absorption, and the optical intensity was 10 mW/cm$^2$. Equations (8) and (9) describe the combined effects of the probe light intensity ($I_{\text{probe}}$) and frequency ($\nu_{\text{probe}}$) on the scale factor. When the probe light intensity is fixed at 20 mW/cm$^2$, changing the probe frequency detuning from −220 GHz to 220 GHz, the response signal ($V$) is detected with calibration magnetic field ($B_x$) of 100 pT rms, and the dependence is shown in Fig. 2(a). The response signal reaches the maximum value when the probe light is blue detuned by about 100 GHz. The experimental data is well fitted with Eq. (9), as shown in Fig. 2(a) with the red solid line. The optimal frequency detuning for maximum signal

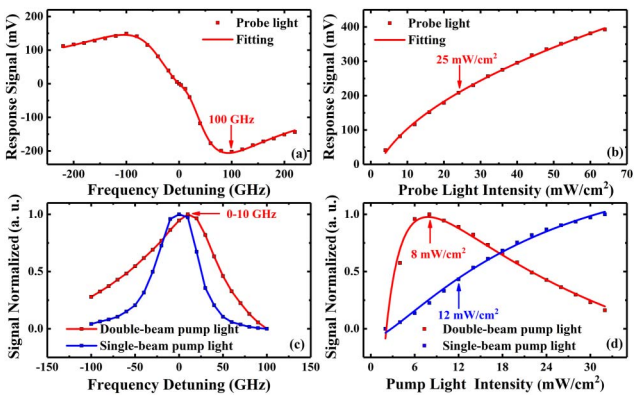


**Fig. 2.** Response signal versus (a) frequency detuning of probe light, (b) light intensity of probe light, (c) frequency detuning of pump light, and (d) light intensity of pump light.

depends on optical depth and pressure-broadening width. By setting $\partial k_2/\partial[(\nu_{\rm pr}-\nu_{D1})/(\Gamma_{D1}/2)]=0$, the maximum scale factor will be obtained when the detuning $(\nu_{\rm probe}-\nu_{D1})$ reaches the optimal value, which is given by

$$\nu_{\rm probe}-\nu_{D1}=\pm\frac{\Gamma_{D1}}{2}\sqrt{\mathrm{OD}(\nu_{D1})+\sqrt[2]{\mathrm{OD}^2(\nu_{D1})+1}}. \quad (11)$$

In Fig. 2(b), the probe light intensity varies from 5 mW/cm$^2$ to 65 mW/cm$^2$, and the probe light frequency is maintained at 100 GHz blue detuning. From Eq. (8), the scale factor is positively correlated with probe light intensity. The response signal increased with probe light intensity, and the experimental data is well fitted in Fig. 2(b) as a red solid line. However, when the light intensity increases above 25 mW/cm$^2$, the corresponding probe light intensity noise increases substantially, resulting in the signal-to-noise ratio not being significantly improved. In the experiment, the probe light intensity of 25 mW/cm$^2$ was adopted.

When analyzing the pump light, the two-mode transimpedance amplifier uses different gains, and therefore, the response signal is divided by the maximum value to be normalized, as shown in Figs. 2(c) and 2(d). For the pump light frequency, the resonance absorption frequency is 377.084 THz ($^{87}$Rb D1 line). Sweeping the pump light frequency near the absorption point with detuning from −220 GHz to 220 GHz, the corresponding response signal curve is detected and shown in Fig. 2(c) on the red line. The response signal is an approximately Lorentzian line shape and reaches the maximum value when the detuning is within 0–10 GHz. When the frequency is maintained near the resonance absorption, the fictitious magnetic field generated by light shifts is effectively suppressed.

In Fig. 2 (d), the pump light intensity varies from 5 mW/cm$^2$ to 65 mW/cm$^2$, and the experimental data is well fitted with Eq. (10), as shown in Fig. 2(d) with the red solid line. The response reaches the maximum when the pump intensity is 8 mW/cm$^2$. As predicted by Eq. (10), the scale factor reaches a maximum when the pumping rate is equal to the transverse relaxation rate ($R_{\rm OP}=R_{\rm rel}$). Since pumping rate is proportional to the intensity of the pump light, $k_3$ reached the maximum under an ideal pump light intensity, which is given by

$$I_{\rm pump}=\frac{h\nu_{\rm pump}}{r_e c f_{D1}}\frac{(\nu_{\rm pump}-\nu_{D1})^2+(\Gamma_{D1}/2)^2}{\Gamma_{D1}/2}\left(R_{\rm SD}+\frac{1}{T_D}\right). \quad (12)$$

In the single-beam mode, the vapor cell temperature and compensation magnetic field settings were consistent with the double-beam mode. The response signal of the single-beam mode measured by PD1 is demodulated with a lock-in amplifier, and the scale factor ($k_{\rm single}\approx k_4k_5k_6$) has the following form:

$$k_4=\eta_2 I_{\rm pump}\gamma^e, \quad (13)$$

$$k_5=e^{-(1-p_z)\mathrm{OD}(\nu_{\rm pump})}, \quad (14)$$

$$k_6=\frac{R_{\rm OP}J_0\left(\frac{\gamma^e B_1}{\omega}\right)J_1\left(\frac{\gamma^e B_1}{\omega}\right)}{(R_{\rm OP}+R_{\rm rel})^2}, \quad (15)$$

where $\eta_2$ is the conversion factor of the PD, $I_{\rm pump}$ is the pump light intensity, and $\nu_{\rm pump}$ is the frequency of the pump light.

The response signal varied with the frequency detuning of the pump light, as shown by the blue line in Fig. 2(c). The response signal reaches a maximum when the pump light frequency remains at the central frequency. The frequency detuning increases, and the response signal gradually becomes weaker.

From Eq. (13), the scale factor is positively correlated with pump light intensity, which satisfies $k_{\rm single}\propto I_{\rm pump}$. In Fig. 2(d) on the blue line, as the intensity increases, the value of the corresponding response signal also increases. The experimental data is well fitted with Eqs. (13) and (15), as shown in Fig. 2(d) with the blue solid line. Although the response signal of the single-beam mode becomes stronger as the pump light intensity increases, the corresponding noise also increases. Optimal performance of the single-beam mode can be achieved when the light intensity reaches 12 mW/cm$^2$.

Figure 3 depicts the response signal of the SERF magnetometer as a function of the temperature from 128°C to 180°C. The two modes have the maximum response value corresponding to the optimal operation temperature. At this temperature, the polarization rate of the alkali-metal atoms is approximately 1/2, and the SERF magnetometer achieves optimal performance. It is worth noting that the optimal temperature of the two modes is different: for the single-beam mode, it is 146°C, and, for the double-beam mode, it is 170°C. The main reason for this difference is that the introduction of the modulation magnetic field increases the transverse relaxation time, making it easier to achieve $R_{\rm rel}=R_{\rm OP}$ in the single-beam mode. In actual use, we can first use the double-beam mode (at 170°C) to calibrate the ambient magnetic field noise, and then use the single-beam mode (at 146°C) to perform the biomagnetic measurement. It pre-evaluates the background magnetic field and effectively reduces power consumption and surface temperature in the MEG system.

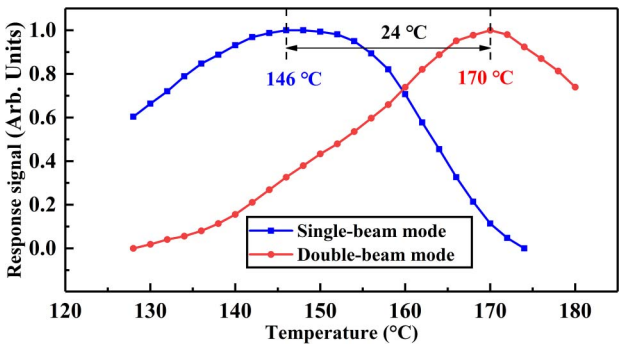


**Fig. 3.** Response signal as a function of temperature at the optimal optical parameters.

### 4.2. Sensitivity and bandwidth

Based on the above analysis and experiments, it can be concluded that the optimal response signal can be obtained by controlling the light parameters and the vapor cell temperature to quickly identify the best sensitivity of the SERF magnetometer system. We apply a 100 pT rms sinusoidal calibration signal at 30 Hz along the $x$ axis and record the frequency spectrum of the magnetometer response for 150 s. The power spectral density is calculated and averaged for 1 Hz bin. The sensitivity noise floors for single-beam and dual-beam modes are shown in blue and red dashed lines in Fig. 4, respectively. The magnetic field sensitivity is higher than 20 $\mathrm{fT/Hz^{1/2}}$ in the single-beam mode and 7 $\mathrm{fT/Hz^{1/2}}$ in the double-beam mode under the previous optimal configuration. Figure 5 shows the normalized frequency response of the single-beam mode and double-beam mode with the 100 pT rms calibration magnetic field. The bandwidths at −3 dBm were 141 Hz and 65 Hz for the single-beam mode and double-beam mode, respectively.

For the mm-level vapor cell, 7 $\mathrm{fT/Hz^{1/2}}$ is the ideal sensitivity. However, when the pump light is blocked, the probe noise of the magnetometer is only 4 $\mathrm{fT/Hz^{1/2}}$, as shown in Fig. 4. Therefore, it can be concluded that 7 $\mathrm{fT/Hz^{1/2}}$ approaches the noise floor of the four-layer mu-metal magnetic-shielding cylinder. According to the physical parameters of the cylinder, the 7 $\mathrm{fT/Hz^{1/2}}$ noise floor is consistent with the theoretical value of the magnetic noise by the Johnson current[29]. Furthermore, we can use the double-beam mode to precisely measure the noise floor of the shielding material, which is another important application for miniaturized SERF magnetometers. The SERF magnetometer mode can be switched arbitrarily for different application scenarios of the sensor. Although the sensitivity in the single-beam mode is poorer than that of the double-beam mode, it is more advantageous in structure and operating temperature and has gradually become a development trend in recent years. The sensitivity and bandwidth are sufficient to meet the needs of biomagnetic measurement[3]. Also, for some special applications, the bandwidth can be extended to 1.8 kHz by closing the loop and increasing the modulated magnetic field frequency[30].

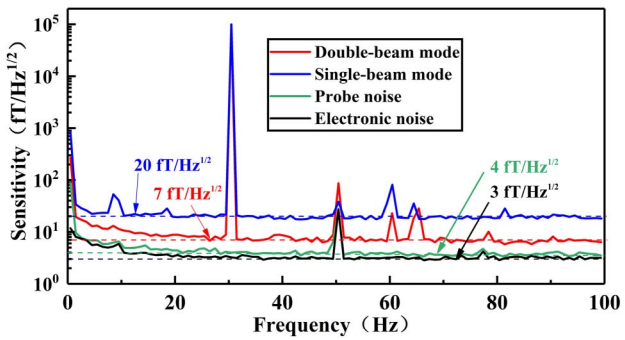


**Fig. 4.** Sensitivity of the SERF magnetometer. The probe noise is recorded by blocking the pump light and turning on the probe light. The electronic noise is recorded by blocking the pump light and probe light.

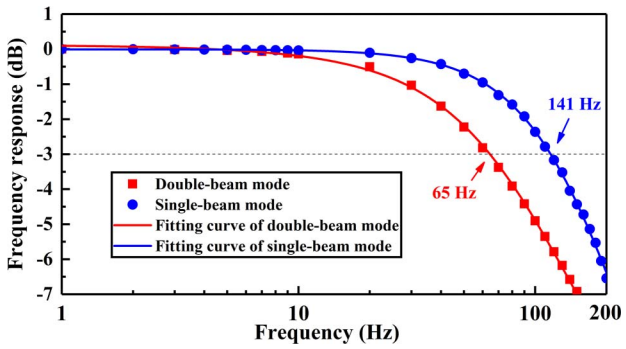


**Fig. 5.** Frequency response of the 100 pT rms calibrated magnetic field at frequency of 1–200 Hz and fitting curve in the single-beam mode and double-beam mode, respectively.

## 5. Conclusion

In summary, we have developed a dual-mode SERF magnetometer with mm-level vapor cells using two Rb D1 line lasers, which can switch between the single-beam modulation mode and the double-beam DC mode for different applications. When operating under appropriate conditions, this SERF magnetometer shows a magnetic field sensitivity of 20 $\mathrm{fT/Hz^{1/2}}$ in the single-beam mode and probe noise of 4 $\mathrm{fT/Hz^{1/2}}$ in the double-beam mode. The noise floor of the multilayer mu-metal magnetic-shielding cylinder was measured to be 7 $\mathrm{fT/Hz^{1/2}}$ in the double-beam mode. Our design provides a method for realizing miniaturized OPMs with multiple functions, including magnetic-shield background noise measurement and medical imaging.

## Acknowledgement

This work was supported by the National Key R&D Program of China (No. 2018YFB2002405) and the National Natural Science Foundation of China (No. 61903013).

## References

1. V. Shah and M. V. Romalis, "Spin-exchange relaxation-free magnetometry using elliptically polarized light," Phys. Rev. A **80**, 013416 (2009).
2. I. K. Kominis, T. W. Kornack, J. C. Allred, and M. V. Romalis, "A subfemtotesla multichannel atomic magnetometer," Nature **422**, 596 (2003).
3. E. Boto, N. Holmes, J. Leggett, G. Roberts, V. Shah, S. S. Meyer, L. D. Muñoz, K. J. Mullinger, T. M. Tierney, S. Bestmann, G. R. Barnes, R. Bowtell, and M. J. Brookes, "Moving magnetoencephalography towards real-world applications with a wearable system," Nature **555**, 657 (2018).
4. H. B. Dang, A. C. Maloof, and M. V. Romalis, "Ultrahigh sensitivity magnetic field and magnetization measurements with an atomic magnetometer," Appl. Phys. Lett. **97**, 151110 (2010).
5. H. H. Nelson and J. R. McDonald, "Multisensor towed array detection system for UXO detection," IEEE Trans. Geosci. Remote Sens. **39**, 1139 (2001).
6. D. Sheng, S. Li, N. Dural, and M. V. Romalis, "Subfemtotesla scalar atomic magnetometry using multipass cells," Phys. Rev. Lett. **110**, 160802 (2013).
7. H. Xia, A. Ben-Amar Baranga, D. Hoffman, and M. V. Romalis, "Magnetoencephalography with an atomic magnetometer," Appl. Phys. Lett. **89**, 211104 (2006).

8. A. P. Colombo, T. R. Carter, A. Borna, Y. Jau, C. N. Johnson, A. L. Dagel, and P. D. Schwindt, "Four-channel optically pumped atomic magnetometer for magnetoencephalography," Opt. Express **24**, 15403 (2016).
9. Y. Yan, G. Liu, H. Lin, K. Yin, and J. Lu, "VCSEL frequency stabilization for optically pumped magnetometers," Chin. Opt. Lett. **19**, 121407 (2021).
10. O. Alem, T. H. Sander, R. Mhaskar, J. LeBlanc, H. Eswaran, U. Steinhoff, Y. Okada, J. Kitching, L. Trahms, and S. Knappe, "Fetal magnetocardiography measurements with an array of microfabricated optically pumped magnetometers," Phys. Med. Biol. **60**, 4797 (2015).
11. S. P. Krzyzewski, A. R. Perry, V. Gerginov, and S. Knappe, "Characterization of noise sources in a microfabricated single-beam zero-field optically-pumped magnetometer," J. Appl. Phys. **126**, 044504 (2019).
12. W. Happer and H. Tang, "Spin-exchange shift and narrowing of magnetic resonance lines in optically pumped alkali vapors," Phys. Rev. Lett. **31**, 273 (1973).
13. I. M. Savukov and M. V. Romalis, "Effects of spin-exchange collisions in a high-density alkali-metal vapor in low magnetic fields," Phys. Rev. A **71**, 023405 (2005).
14. J. Tang, Y. Zhai, L. Cao, Y. Zhang, L. Li, B. Zhao, B. Zhou, B. Han, and G. Liu, "High-sensitivity operation of a single-beam atomic magnetometer for three-axis magnetic field measurement," Opt. Express **29**, 15641 (2021).
15. H. B. Dang, A. C. Maloof, and M. V. Romalis, "Ultrahigh sensitivity magnetic field and magnetization measurements with an atomic magnetometer," Appl. Phys. Lett. **97**, 151110 (2010).
16. A. P. Colombo, T. R. Carter, A. Borna, Y. Y. Jau, C. N. Johnson, A. L. Dagel, and D. D. Schwindt, "Four-channel optically pumped atomic magnetometer for magnetoencephalography," Opt. Express **24**, 15403 (2016).
17. R. Wyllie, M. Kauer, R. T. Wakai, and T. G. Walker, "Optical magnetometer array for fetal magnetocardiography," Opt. Lett. **37**, 2247 (2012).
18. D. Y. Ma, J. X. Lu, X. J. Fang, K. Yang, K. Wang, N. Zhang, B. C. Han, and M. Ding, "Parameter modeling analysis of a cylindrical ferrite magnetic shield to reduce magnetic noise," IEEE Trans. Ind. Electron. **69**, 991 (2021).
19. J. Osborne, J. Orton, and O. Alem, "Fully integrated standalone zero field optically pumped magnetometer for biomagnetism," Proc. SPIE **10548**, 105481G (2018).
20. V. P. Gerginov, L. Li, M. Gerginov, S. Krzyzewski, and S. Knappe, "Microfabricated magnetometers for imaging and communication," Proc. SPIE **11296**, 112963C (2020).
21. O. Alem, T. Sander, R. Mhaskar, J. Leblanc, H. Eswaran, and U. Steinhoff, "Fetal magnetocardiography measurements with an array of microfabricated optically pumped magnetometers," Phys. Med. Biol. **60**, 4797 (2015).
22. O. Alem, R. Mhaskar, J. Ricardo, D. Sheng, and S. Knappe, "Magnetic field imaging with microfabricated optically-pumped magnetometers," Opt. Express **25**, 7849 (2017).
23. S. J. Seltzer, "Developments in alkali-metal atomic magnetometry," Ph.D. thesis (Princeton University, 2008).
24. J. Lu, Z. Qian, and J. Fang, "A fast determination method for transverse relaxation of spin-exchange-relaxation-free magnetometer," Rev. Sci. Instrum. **86**, 043104 (2015).
25. M. P. Ledbetter, I. M. Savukov, V. M. Acosta, D. Budker, and M. V. Romalis, "Spin-exchange-relaxation-free magnetometry with Cs vapor," Phys. Rev. A **77**, 033408 (2008).
26. T. M. Tierney, N. Holmes, S. Mellor, J. D. López, and G. R. Barnes, "Optically pumped magnetometers: from quantum origins to multi-channel magnetoencephalography," NeuroImage **199**, 598 (2019).
27. R. E. Slocum and B. I. Marton, "Measurement of weak magnetic fields using zero-field parametric resonance in optically pumped $He_4$," IEEE Trans. Magn. **9**, 221 (1973).
28. C. Cohen-Tannoudji and J. Dupont-Roc, "Experimental study of Zeeman light shifts in weak magnetic fields," Phys. Rev. A **5**, 968 (1972).
29. S. K. Lee and M. V. Romalis, "Calculation of magnetic field noise from high-permeability magnetic shields and conducting objects with simple geometry," J. Appl. Phys. **103**, 084904 (2008).
30. J. Tang, Y. Zhai, B. Zhou, B. Han, and G. Liu, "Dual-axis closed loop of a single-beam atomic magnetometer: toward high bandwidth and high sensitivity," IEEE Trans. Instrum. Meas. **70**, 1504808 (2021).